Environment Protection Engineering

Vol. 51 2025 No. 1

DOI:10.37190/epe250103

GUIHUA HU (ORCID: 0000-0003-0217-607X)[1, 2]
KUNPENG CHEN (ORCID: 0009-0007-0741-3253)[3]
MIMI CHEN (ORCID: 0009-0007-7360-2271)[1]

NUMERICAL SIMULATION AND MULTI-OBJECTIVE OPTIMIZATION OF ULTRA-LOW NITROGEN BURNERS FOR ETHYLENE CRACKING FURNACES

Coupled numerical simulation and multi-objective optimization for ultra-low nitrogen burners of ethylene cracking furnaces using a fast response surrogate model for combustion are proposed. Firstly, based on simplified reaction mechanisms involving 29 species and 164 reactions, a computational fluid dynamics (CFD)-coupled model for turbulent combustion is established. Secondly, a multi-objective optimization scheme based on a strong generalization-based surrogate model is developed for ultra-low nitrogen burners of ethylene cracking furnaces. The results show that a set of optimal operating parameters for the cracking furnace, i.e., the excess air coefficient of 1.07, the fuel gas flow rate of 0.192 kg/s, and the air preheating temperature of 380 K, is obtained. The optimal NO_x emission concentration decreased from 75.38 mg/m^3 of the original scheme to 71.2 mg/m^3, i.e., a decrease of 5.55%. The thermal efficiency of the firebox increased from 43.82% of the original scheme to 44.49%, i.e., an increase of 1.53%, which provides theoretical guidance for energy conservation and emission reduction of cracking furnaces.

1. INTRODUCTION

The optimization design of ultra-low nitrogen burners plays an important role in controlling pollutant emissions in industry and is an important part of green, environ-

[1]Key Laboratory of Smart Manufacturing in Energy Chemical Process of Ministry of Education, East China University of Science and Technology, Shanghai 200237, China, corresponding author G. Hu, email address: huguihua@ecust.edu.cn

[2]Engineering Research Center of Process System Engineering, Ministry of Education, East China University of Science and Technology, Shanghai 200237, China.

[3]CIBFINTECH, No. 2977 Chuansha Road, Pudong New Area, Shanghai 200131, China.

mentally friendly, and sustainable development. However, combustion technology optimization focuses on improving final product processing and energy conservation, and little attention is paid to NO_x emission reduction indicators. With the development of green intelligent manufacturing, multi-objective optimization research that considers both product yield and pollutant emissions has received widespread attention [1, 2].

With the rapid development of computational fluid dynamics (CFD) simulation technology, simulation models can be used to predict various systems performances for various engineering problems, and the cost of time and economy for research has been greatly reduced. However, to pursue the accuracy of numerical simulation, simulation models have become increasingly complex, and the computational expense has grown several times or even tens of times. For example, in the combustion optimization of cracking furnaces, performing a simulation requires analyzing thousands of Navier –Stokes equations with source terms, and optimization problems often require several simulations to achieve good results [3]. Even for advanced modern computers, such computational complexity is too large, and the high time cost seriously limits the application of excellent simulation models in engineering problems. At the same time, CFD simulation lacks globality, and it is not easy to achieve a comprehensive relationship between input and output solely through simulation experiments. To solve these problems, an effective method is to establish a combustion surrogate model for the cracking furnace. Common surrogate modeling techniques include the response surface methodology (RSM) [4], Kriging model [5], support vector regression (SVR) model [6], back-propagation (BP) neural network [7], radial basis function (RBF) neural network [8], convolutional neural network (CNN) [9], and the application of these surrogate models [10]. Aboaba et al. [11] used intelligent algorithms to construct a surrogate model for a high-pressure combustion facility exceeding 400 W. The model was created using only eight CFD simulation runs, which can replicate the detailed distribution of pressure, temperature, and flue gas component concentration in the CFD simulation model with less than 10% error within just a few seconds. Yao et al. [12] proposed a Kriging-assisted reference vector guided evolutionary algorithm (K-RVEA) optimization framework, which optimized the parameters of the combustion CFD model and studied the effect of burner structure on NO_x emissions.

In actual production, it is often faced with the problem of simultaneously optimizing two or more objectives, and these optimization objectives have mutual constraints [13], called multi-objective optimization problems [14]. Previous experts often relied on experience to adjust parameters for optimal production performance. On the one hand, this made the obtained optimal value easily fall into local optimal solutions. On the other hand, a shutdown is often required for adjustment due to inaccurate predictions, resulting in huge economic losses [15]. With the rapid development of computer technology, mathematical analysis, and machine learning algorithms, the use of artificial intelligence algorithms for data-driven modeling and optimization has provided new solutions

for industrial problems. Menzel et al. [16] used the non-dominated sorting genetic algorithm II (NSGA-II) algorithm and the multi-objective evolutionary algorithm based on the decomposition (MOEA/D) algorithm for multi-objective optimization of engine thermal efficiency, seeking the optimal valve opening and closing conditions. After comparative analysis, the MOEA/D algorithm has more non-dominated solution sets, larger super volumes, and less computational time. Sener and Gül [17] optimized the geometric shape of compression ignition engines based on CFD technology and used a multi-objective genetic algorithm (MOGA) to automatically change and design optimization parameters. The final established geometric dimensions and injection parameters significantly reduced NO_x and smoke emissions, while improving fuel efficiency.

Accurately establishing a combustion reaction mechanism model for NO_x emissions is the basis for optimizing the design of ultra-low nitrogen burners. The combination of surrogate models and CFD to improve the quality and prediction speed of the training dataset is becoming a new trend. However, research on surrogate models for turbulent combustion processes in ultra-low nitrogen burners of ethylene cracking furnaces has not been reported in the literature. This article aims to propose a multi-objective optimization design method for ultra-low nitrogen burners that is suitable for industrial practice. Specifically, a comprehensive application of CFD modeling, simplified reaction kinetics mechanism, surrogate model, and multi-objective optimization methods are used to construct the optimization design of operating parameters for the ultra-low nitrogen burner of the cracking furnace. Firstly, a coupled CFD model for turbulent combustion in a cracking furnace is established. The NO_x generation mechanism adopts GRI-Mech 3.0 [18], and its NO_x generation in the cracking furnace mainly consists of thermal NO and prompt NO. The impact of combustion characteristics in the cracking furnace on NO_x generation is analyzed. Secondly, the direct relationship graph (DRG) combined with the computational singular perturbation (CSP) method is applied to reasonably simplify the detailed reaction kinetics mechanism of GRI3.0 methane combustion, which can improve calculating speed by 60%. Thirdly, by comparing the simulation and generalization capabilities of the RBF neural network and SVR model, the RBF neural network is selected as the surrogate model of ultra-low nitrogen burners of ethylene cracking furnaces. Finally, the NO_x emission concentration and thermal efficiency of the firebox are optimized by NSGA-II, and the optimal operating parameter scheme that meets the NO_x emission reduction and energy conservation indicators is obtained.

2. CFD SIMULATION

2.1. FURNACE GEOMETRY AND CONDITION BOUNDARY

Because this paper mainly studies the generation of pollutants during the combustion process, the reactor tubes are not considered. The geometric model of the cracking

furnace in this study is shown in Fig. 1a. The total size is 18.94 m (length) × 3.56 m (width) × 13.707 m (height), and 36 non-premixed multi-stage fuel bottom burners are installed near the walls on both sides. Both sides of the furnace wall are equipped with 48 premixed burners. The reactor tubes are divided into inlet and outlet ones with different diameters and are vertically suspended in the center of the furnace. Each multi-stage fuel burner is equipped with one preheating air inlet, one primary fuel gas inlet for main combustion, and four secondary fuel gas inlets for auxiliary combustion. Two rows of 48 premixed burners are evenly arranged on the walls on both sides of the furnace, with the flue gas outlet located at the top of the furnace. To simplify the calculation, this paper uses a 1/6 furnace structure based on the principle of symmetry for numerical simulation and uses Gambit to mesh the cracking furnace, as shown in Fig. 1b.

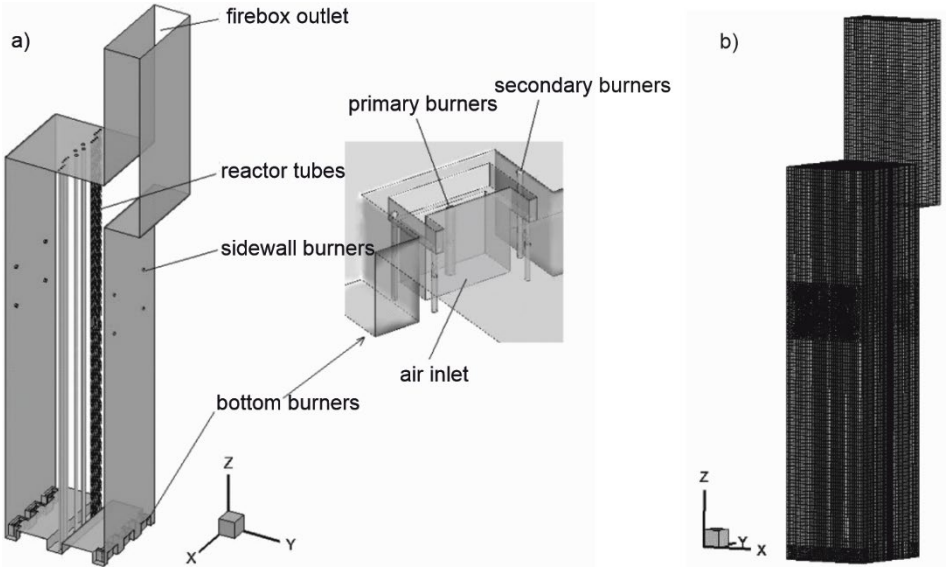

Fig. 1. Geometry (a) and mesh (b) of the ethylene cracking furnace

The inner wall of the furnace is mainly composed of refractory bricks, mixed with some insulation cotton and refractory materials to maintain temperature. It can be defined as the heat flux wall surface, with a value of 972 W/m^2. The flow and heat transfer of fluid near the wall is approximated by the standard wall function. The initial outer wall temperature of the reactor tube is assumed to be based on industrial production practice and operational experience. The initial temperature boundary conditions are imported into Fluent 19.1 [19] for calculation through a user-defined function (UDF). The fuel gas inlet flow rate, air inlet flow rate, and corresponding temperature, pressure, and hydraulic diameter of the bottom burners and sidewall burners are determined based on actual industrial production. The operating conditions of the ethylene cracking furnace are shown in Table 1.

Table 1

Operating conditions of ethylene cracking furnace

Item	Mass flow rate [kg/s]	Temperature [K]	Gauge pressure [Pa]	Hydraulic diameter [m]
Bottom burners	0.1813	300	120 000	0.024
Sidewall burners	0.6682	300	120 000	0.0953
Air inlet	3.3842	298	101 325	0.246
Furnace outlet	–	–	–50	–
Fuel composition, wt. %				
CH_4	97.686			
H_2	0.51686			
CO	0.89768			
C_2H_4	0.89946			

2.2. NUMERICAL MODELS

Flow model. Reynolds-averaged Navier–Stokes equations are used for the turbulent flow model of the ethylene cracking furnace, closed with the standard k–ε model [20]. Control equations include mass, momentum, energy, and species equations. These equations have similarities in form and can be expressed in the following general form:

$$\frac{\partial(\rho\phi)}{\partial t}+\frac{\partial\left(\rho U_j\phi\right)}{\partial x_j}=\frac{\partial}{\partial x_j}\left(\Gamma_\phi\frac{\partial\phi}{\partial x_j}\right)+S_\phi \tag{1}$$

where ρ is gas density, ϕ represents the dependent variables, t is time, U_j is the velocity component in the jth direction, x_j is the coordinate direction in the jth direction, Γ_ϕ the generalized diffusion coefficient, S_ϕ is the source term.

Combustion model. The eddy dissipation concept (EDC) model [21] is used to establish the combustion model. Due to the slow reaction rate of NO_x and CO emissions in cracking furnace combustion, the EDC model assumes that molecular mixing and subsequent reactions occur in a small turbulent structure on the Kolmogorov scale, where turbulent kinetic energy is dissipated into heat. Considering that the EDC model considers the detailed combustion chemical reaction mechanism in the turbulent structure, it can more accurately track the chemical reaction process, and its coupling with the turbulent model is more in line with the actual physical phenomena in the cracking furnace. The net rate of production of species by chemical reaction R_i in the conservation equation for the mean species i, Eq. (1), is calculated as

$$R_i=\frac{\rho\left(\xi^*\right)^2}{\tau^*\left(1-\left(\xi^*\right)^3\right)}\left(Y_i^*-Y_i\right) \tag{2}$$

where the asterisk denotes fine-scale quantities, τ^* is the time scale, Y_i is the mass fraction of species i, Y_i is the fine-scale species mass fraction after reacting over time τ^*. ξ is the length fraction of the fine scales.

$$\tau^* = 0.4082\left(\frac{\nu}{\varepsilon}\right)^{1/2} \tag{3}$$

$$\xi^* = 2.1377\left(\frac{\nu\varepsilon}{k^2}\right)^{1/4} \tag{4}$$

where ν is kinematic viscosity, k is turbulent kinetic energy, ε is the dissipation rate of turbulent kinetic energy.

NO model. In this study, the detailed reaction kinetics mechanism of GRI 3.0 methane combustion is used to establish the combustion reaction kinetics model of the ethylene cracking furnace. The main fuel is natural gas, which itself does not contain nitrogen elements, so fuel NO_x does not need to be considered. Prompt NO_x is mainly generated by the reaction of N_2 in the combustion air and hydrocarbons in areas with fuel-rich and low-temperature. The production amount in the cracking furnace combustion is very small. Thermal NO_x is produced by the high-temperature oxidation of N_2 in the air. In flames with a chemical equivalence ratio of less than 1, the main region of NO generation is at the rear end of the flame. Zeldovich [22] first proposed the reaction mechanism of thermal NO_x. The main chain reactions from high-temperature oxidation of N_2 to formation of NO_x are as follows:

$$N_2 + O \rightleftharpoons NO + N \tag{5}$$

$$N + O_2 \rightleftharpoons NO + O \tag{6}$$

When there is an excess of fuel, a third reaction needs to be added:

$$N + OH \rightleftharpoons NO + H \tag{7}$$

Radiation model. In the ethylene cracking furnace, the main form of heat transfer is radiation, which is modeled using a discrete ordinate (DO) radiation model [23].

$$\nabla\cdot\left(I(\vec{\mathbf{r}},\vec{\mathbf{s}})\vec{\mathbf{s}}\right)+\left(\alpha+\sigma_s\right)I\left(\vec{\mathbf{r}},\vec{\mathbf{s}}\right)=\alpha n^2\frac{\sigma T^4}{\pi}+\frac{\sigma_s}{4\pi}\int_0^{4\pi} I\left(\vec{\mathbf{r}},\vec{\mathbf{s}}'\right)\Phi\left(\vec{\mathbf{s}}\cdot\vec{\mathbf{s}}'\right)d\Omega' \tag{8}$$

where $\vec{\mathbf{r}}$ is position vector, $\vec{\mathbf{s}}$ is direction vector, $\vec{\mathbf{s}}'$ is scattering direction vector, s is path length, α is absorption coefficient, n is refractive index, σ is the Stefan–Boltzmann

constant (5.67×10^{-8} W/(m^2·K^4)), σ_S is scattering coefficient, I is radiation intensity, T is temperature, Φ is phase function, Ω' is solid angle.

The weighted-sum-of-gray-gases model (WSGGM) is used to calculate the radiation characteristics of flue gas [24]. This model divides the emissivity of the real gas into the weighted sum of the emissivity of several gray gases and a transparent gas, which has high computational accuracy and efficiency.

2.3. NUMERICAL METHOD AND NUMERICAL SIMULATION

For discrete schemes such as mass, momentum, and energy, a second-order upwind scheme is used, and the flow field calculation uses the semi-implicit solution of the pressure simultaneous equation (SIMPLE). Except for energy and radiation equations, the residual convergence standard is 10^{-6}, and all other equations have residual convergence standards of 10^{-3}.

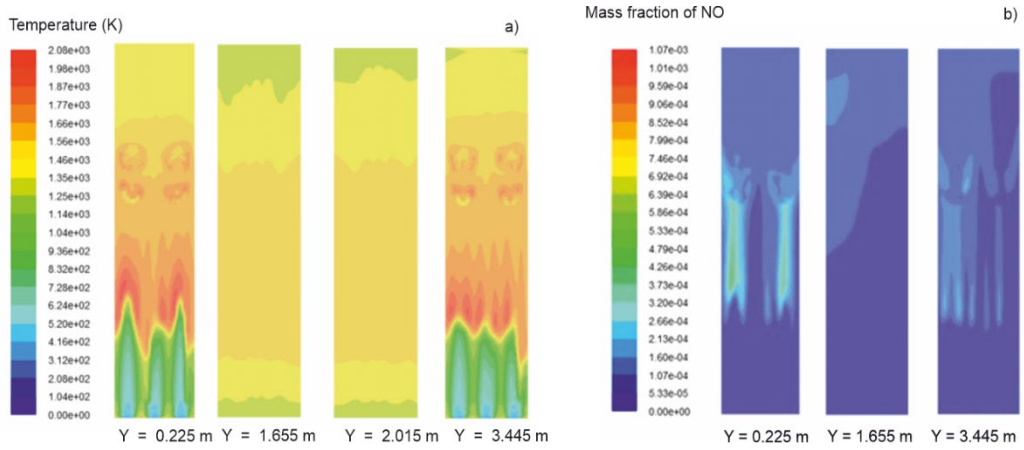

Fig. 2. Flue gas temperature contour (a) and mass fraction of NO contour along the width direction of the furnace (b)

Figure 2a shows the flue gas temperature contour at different sections along the width of the furnace. At the bottom of the furnace, the poor mixture of high-velocity fuel gas and air results in incomplete combustion, which reduces heat release, leading to a low flue gas temperature. In the middle of the furnace, the fuel gas velocity decreases, and the air and fuel mix well, resulting in violent reactions and a large amount of heat release. The mass fraction of NO contour along the width is shown in Fig. 2b. The main generation area of NO in the furnace is around the height of 4–6 m. In this area, the fuel gas and air mix well, and the combustion reaction is intense. The local temperature in the furnace increases sharply, and the nitrogen in the air is oxidized at high temperatures, resulting in a large amount of thermal NO.

Table 2

Simulation results and industrial data

	Industrial data	Simulation data
Flue gas outlet temperature, °C	1124	1137
Excess oxygen ratio, wt. %	1.77	1.60
NO_x emission concentration, mg/m^3	78.08	75.38

Table 2 shows simulation results and industrial data. The simulated temperature of outlet flue gas, excess oxygen ratio and NO_x emission are in agreement with the industrial data. It shows that the simulation results are reliable. The results can be used to analyze the velocity, temperature, and species concentration distributions in the cracking furnace.

3. SIMPLIFICATION OF THE COMBUSTION REACTION MECHANISM

3.1. SIMPLIFIED MODEL OF REACTION KINETICS

In the detailed reaction kinetics mechanism for methane combustion, GRI-Mech 3.0 which contains 53 species, and 325 reactions is currently the most widely used. However, in the simulation of the cracking furnace mentioned above, the turbulent combustion model coupled with the numerical calculations of the reaction kinetics mechanism takes too long. Due to the large number of components and significant time scale differences in the detailed reaction kinetics mechanism, this article first uses the DRG method to simplify the framework of the GRI-Mech 3.0 detailed reaction kinetics mechanism and then uses the CSP method to remove some reactions from the time scale to eliminate the "rigidity" problem of the reaction system. Therefore, it is proposed to use the DRG method combined with the CSP method to simplify the detailed reaction mechanism and verify the calculation results by comparing it with the detailed mechanism in a 0-dimensional homogeneous burner.

For the DRG method, the determination of initial species is crucial for reaction simplification. CH_4, CO, CO_2, and O_2 which have a significant impact on the concentration of methane combustion products are selected as the initial species. Additionally, because this paper aims to achieve an accurate prediction of NO_x, NO, and N_2 are also set as the initial species. The generation rate of each species in each elementary reaction is calculated in a 0-dimensional homogeneous combustion model by using Chemkin [25] and exported in the form of an Excel file. According to Eq. (9), the normalized contribution of the remaining species B to the production rate of the initial species A, R_{AB}, is individually calculated in the detailed reaction mechanism. If the R_{AB} of a species for all initial species is less than the threshold ε, this species can be regarded redundant, and all elementary reactions it participates in can be removed.

$$R_{AB} = \frac{\sum_{i=1}^{l} \left| \nu_{A,i} \omega_i \delta_{Bi} \right|}{\sum_{i=1}^{l} \left| \nu_{A,i} \omega_i \right|} \tag{9}$$

where $\delta_{BI} = 1$ if the ith elementary reaction involves species B, $\delta_{BI} = 0$ otherwise. $\nu_{A,i}$ is the stoichiometric coefficient of species A in the ith reaction, ω_i is the net reaction rate of the ith reaction.

Considering the simplification time and the accuracy of simplification results, the threshold value is $\varepsilon = 0.01$. After the above process, 18 components including CH_2OH, CH_3OH, C_2H_5, C_2H_6, CH_2CO, CH_2CHO, NH_2, and 115 related elementary reactions are removed, resulting in a simplified mechanism consisting of 35 species and 210 reactions.

Next, the CSP method is used to further reduce the simplified reaction kinetics mechanism mentioned above. For a reaction system containing N unknown quantities and R reactions, the N system variables can be represented by an N-dimensional column vector $y = (y^1, y^2, ..., y^N)^T$, which includes physical quantities such as temperature and chemical composition. The governing ordinary differential equation can be expressed as:

$$\frac{dy}{dt} = g(y, t) \tag{10}$$

where $g(y, t)$ is the sum of contributions from the R elementary reactions:

$$g(y, t) = \sum_{r=1}^{R} s_r F^r(y, t) \tag{11}$$

where s_r and $F^r(y, t)$ are the generalized stoichiometric vector and reaction rate of the rth elementary reaction, respectively. The assumption is that $a_n(t)$ is a set of N linearly independent column basis vectors, and $b^n(t)$ is a set of N inverse row basis vectors, where $b^i(t) \cdot a_i(t) = \delta_j^i$. Then, $g(y, t)$ can be expressed as the sum of N reaction modes:

$$g(y,t) = \sum_{n=1}^{N} a_n(t) f^n(y,t) \tag{12}$$

$$f^n(y,t) \equiv b^n(t)\, g(y,t) = \sum_{r=1}^{R} B_r^n F^r, \quad B_r^n = b^n(t) S_r \tag{13}$$

where a_n and f^n are the direction and amplitude of the nth mode, respectively, and their physical meanings are the effective generalized stoichiometric vector and effective reaction rate of the nth mode, respectively. B_r^n is called the augmented stoichiometric coefficient.

The participation index P_r^n indicates the degree of participation of the ith basic reaction in the nth mode

$$P_r^n \equiv \frac{B_r^n F^r}{\sum_{r'=1}^{R} \left| B_{r'}^n F^{r'} \right| + O\left| \frac{b^n \Delta y}{\Delta t} \right|} \tag{14}$$

where Δy is the allowable error vector of the unknown quantity, and Δt is the time scale.

If the participation index of an elementary reaction is less than a given threshold ε_p, it can be considered a reaction with weak participation and can be removed.

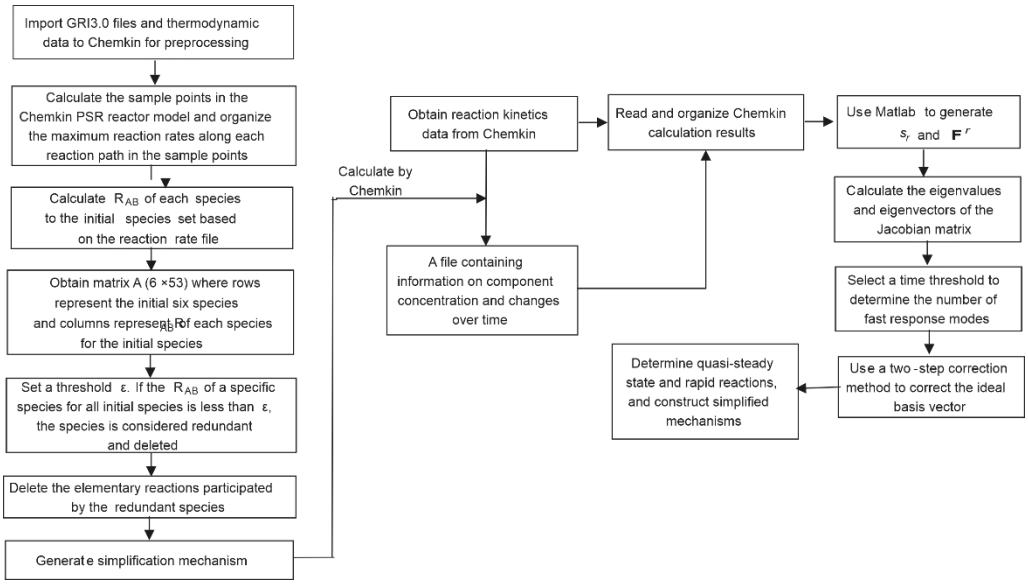

Fig. 3. Simplified calculation process for GRI-Mech3.0 reaction mechanism

After simplifying the primary skeleton reaction mechanism, the elementary reactions containing components with smaller reaction contribution rates have been removed. The simplified mechanism based on the DRG method is introduced into a 0-dimensional homogeneous burner for simulation combustion, and chemical reaction kinetics data, including elementary reaction rate, stoichiometry coefficient, and component concentration, are obtained. The stoichiometric number matrix and reaction rate corresponding to each elementary reaction are imported into Matlab to obtain s_r and F^r. Proceed to the next step, the Jacobian matrix of the reaction system is calculated. Next, the Chemkin species concentration file is used to determine the start and end time of the reaction, and the species concentration at the time is brought into the Jacobian matrix. The eigenvalues and eigenvectors of the Jacobian matrix at that time are solved. The

number of fast modes is determined based on these eigenvalues, and the eigenvectors are considered trial basis vectors. Then, the correction method provided by the CSP theory is used to correct the trial basis vectors, and thereby the Jacobian matrix region is diagonalized and the decoupling of fast and slow modes is achieved. Finally, the modified basis vectors are used to obtain a fast spatial mapping matrix, and the quasi-steady species are identified. These identified quasi-steady species and their involved elementary reactions are removed from the reaction system. We set the threshold values of time scale, $\Delta t = 0.02$, and threshold values of P_r^n, $\varepsilon_p = 0.01$, with an allowable error Δy of 10%. Six quasi-steady state species such as C_2H_3, CH_3O, HCN, and 46 different important elementary reactions are further identified. After removing these components and reactions, the primary mechanism is simplified to a reaction mechanism containing 164 reactions of 29 species. The calculation process is shown in Fig. 3.

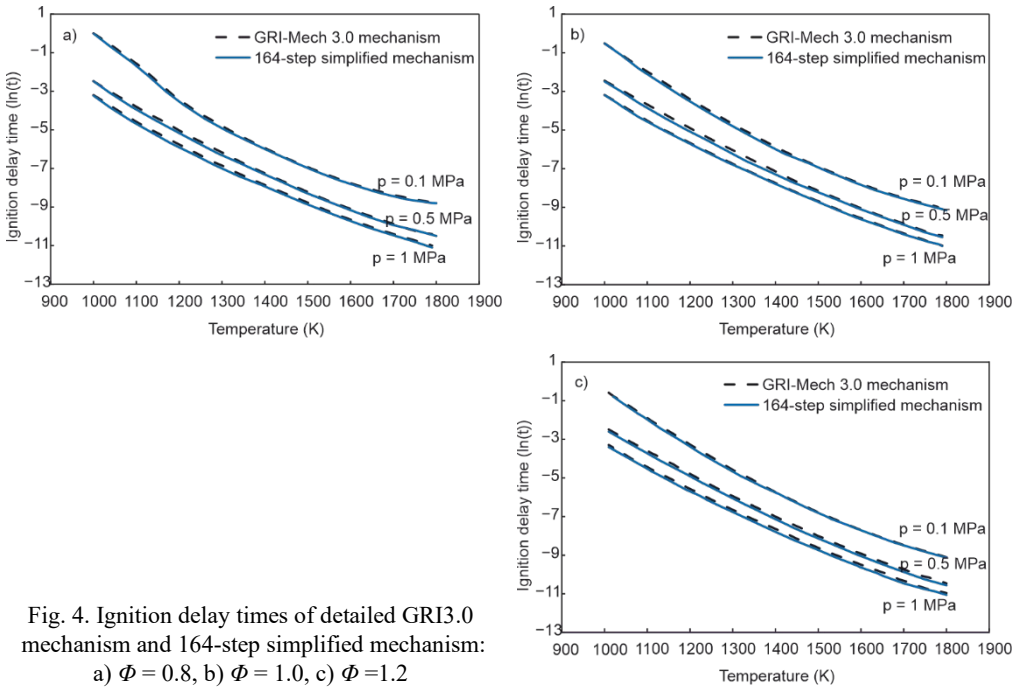

Fig. 4. Ignition delay times of detailed GRI3.0 mechanism and 164-step simplified mechanism: a) $\Phi = 0.8$, b) $\Phi = 1.0$, c) $\Phi = 1.2$

To verify the accuracy of the simplified mechanism, a 0-dimensional homogeneous combustion model of Chemkin software is used to compare the detailed reaction mechanism of GRI3.0 with the established 164-step simplified reaction mechanism. The initial equivalence ratios are 0.8, 1, and 1.2, pressures are 0.1, 0.5, and 1 MPa, and temperatures are varied between 1000 and 1800 K. The ignition delay time on the vertical axis is dimensionless using the natural logarithm of ignition delay time. The test results are shown in Fig. 4. The results show that the simplified mechanism has good reliability

under a wide range of operating conditions, and the average error of ignition delay time is less than 5%.

3.2. VERIFICATION FOR FLAME D

In Flame D [26], the fuel stream containing one-quarter methane and three-quarters air is ejected from the main jet at a velocity of 49.6 m/s. The pilot jet is an annular stream that tightly surrounds the main jet with an outer diameter of 18.2 mm and an inlet velocity of 11.4 m/s. The air co-flow surrounds the pilot jet with a velocity of 0.9 m/s. The structures and operating conditions of Flame D are shown in Table 3.

Table 3

Structures and operating conditions of Flame D

Item	Main jet	Pilot jet	Air co-flow
Diameter/length×width, mm	7.2	18.2	300×300
Temperature, K	294	1880	291
Velocity, m/s	49.6	11.4	0.9
Components (mass fraction)			
CH_4	0.156	0	0
O_2	0.197	0.054	0.23
N_2	0.647	0.742	0.77
CO_2	0	0.110	0
H_2O	0	0.094	0

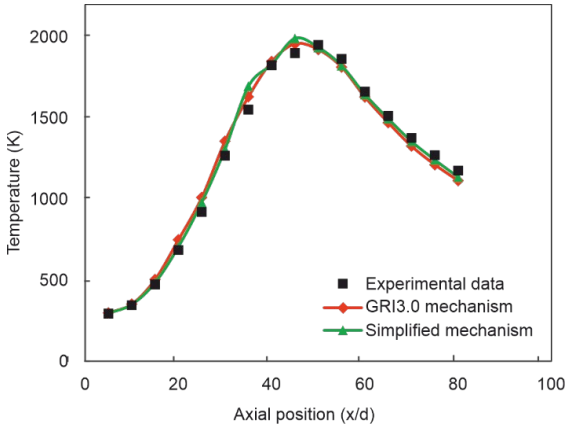

Fig. 5. Temperature along the axial direction

This paper adopts the standard k–ε turbulent flow model and EDC combustion model, which are respectively combined with the detailed reaction kinetics mechanism of GRI-Mech 3.0 and the simplified mechanism established above to simulate the Flame D

combustion process. In the following description, the axial length is dimensionless using the diameter d of the main jet. Figure 5 shows temperature distribution along the central axis. It can be seen that the average flame temperature reaches its peak at about $x/d = 45$, approximately 2000 K. At the same time, in areas with high-temperature gradients, the average flame temperature of simplified mechanism is slightly higher than that of experimental data, but the highest flame temperature of the two is highly consistent with its average temperature after combustion stability.

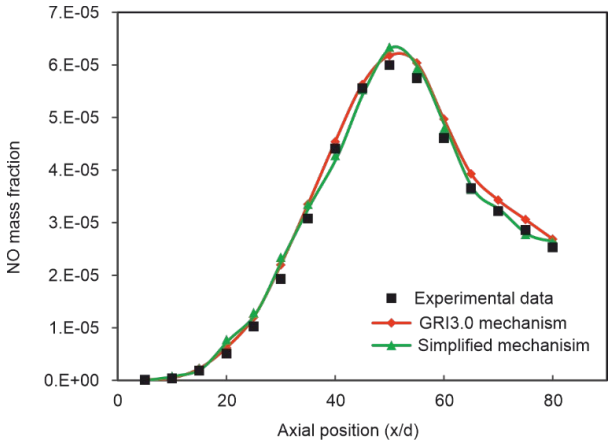

Fig. 6. NO mass fraction along the axial direction

Figure 6 shows the distribution of the NO mass fraction for two simulations and experimental data along the central axis. The concentration of NO first increases and then decreases with the change of combustion adequacy, with a maximum value at x/d equal ca. 50. Because Flame D is a diffusion flame, there are reaction layers with high temperatures even in the vicinity of the fuel nozzle exit, which produces NO through the Zeldovich mechanism. The decrease in NO concentration in the far field is probably due to the dilution resulting from the entrainment of ambient air. From this, it can be verified that the simplified mechanism containing 164 steps of elementary reactions has good computational accuracy in three-dimensional simulation calculations. The calculation speed of the coupled simplification mechanism has increased by about 60%, greatly improving the efficiency of the simulation.

4. OPTIMIZATION OF ULTRA-LOW NITROGEN BURNERS

4.1. MULTI-OBJECTIVE OPTIMIZATION STRATEGY

Pollutant emissions and thermal efficiency of the firebox are two important performance indicators of ethylene cracking furnace. Numerous studies and practices have

shown that the yield of cracking products ethylene is directly proportional to the average coil outlet temperature (COT) of the reactor tube within a considerable temperature range [27, 28]. The heat load of the firebox is an important factor affecting COT. According to the NO_x generation mechanism, the strategy of ultra-low nitrogen combustion tends to reduce the temperature of the main combustion zone as much as possible, which reduces the heat load of the firebox and affects the product yield. Thus there is often a mutually restrictive relationship between the amount of NO_x generated and the thermal efficiency of the firebox. To solve this problem, this paper aims to optimize the performance of the cracking furnace through multi-objective optimization research. Therefore, the decision variables are necessary that affect the combustion of the cracking furnace and the target variables to be optimized. The combustion air is an important factor affecting the emission of pollutants from cracking furnaces [29]. On the one hand, appropriately increasing the air preheating temperature in the cracking furnace will promote fuel combustion, reduce chemical incomplete combustion losses, and improve the thermal efficiency of the cracking furnace [30, 31], but increasing the air preheating temperature will also increase NO emissions. To achieve the effect of ensuring the heat demand of the cracking furnace while reducing NO, it is necessary to seek an optimal air preheating temperature to achieve a balance between the two needs. On the other hand, under low excess air coefficient, the fuel will fully burn, which not only reduces the NO generation rate but also improves the thermal efficiency of the cracking furnace. However, if the excess air coefficient is too low, it will increase the CO generation rate and reduce thermal efficiency, so there is a minimum limit to the excess air coefficient. Thus the study selects the excess air coefficient, fuel gas flow rate, and air preheating temperature as decision variables.

The efficiency of the reactor tube absorbing heat largely represents the thermal efficiency of the firebox. Due to the difficulty in simulating the convection section of the cracking furnace, this paper uses the thermal efficiency of the firebox to characterize the energy proportion of fuel gas supply to the reactor tube. The NO_x emission concentration and thermal efficiency of the firebox are selected as the optimization target variable to achieve higher production efficiency under low NO_x emission. The thermal efficiency of the firebox η_f is:

$$\eta_f = \frac{Q_{\text{comb}} + Q_{\text{in}} - Q_{\text{out}} - Q_{\text{furn}}}{Q_{\text{comb}}} \tag{15}$$

where Q_{comb} is the heat provided by the complete combustion of the fuel gas, Q_{in} is the heat required for preheating air, Q_{out} is the removed heat from high-temperature flue gas, Q_{furn} is heat loss from the surface of the furnace wall.

4.2. DESIGN OF EXPERIMENT

The key to building a surrogate model is to train the model using information from known sample points and predict unknown points. Choosing appropriate experimental

design methods to determine sample points is a key step in the process of constructing surrogate models. The experimental design based on Latin hypercube sampling (LHS) can balance the influence of each factor at various levels, and use non-folding design conditions to reduce the design space, making the samples uniform and efficient within a certain size range.

According to the existing model combined with industrial production practice, the range of fuel gas flow rate is between 0.16 and 0.24 kg/s, the range of excess air coefficient is between 1.0 and 1.2, and the range of air preheating temperature is between 300 and 400 K. To ensure that the design points are independent of each other and as close as possible to the space provided by the design variables, the LHS method is used to select sample points in the sample space. The turbulent combustion coupling model established in Section 2.2 is used to perform CFD numerical simulation on the sample points, laying the foundation for the construction of the surrogate model in the following text.

4.3. SURROGATE MODELS FOR RAPID RESPONSE TO COMBUSTION

RBF neural networks and SVR models have excellent performance in dealing with nonlinear problems and are more suitable for small sample problems, especially when dealing with combustion problems in engineering [32, 33]. These two methods have been widely used, so they are used for this study.

4.3.1. RBF NEURAL NETWORK

The basic idea of RBF neural networks is to map the input space into a high-dimensional space through a set of radial basis functions, thereby achieving classification or regression. 90 sample points under different operating parameters are selected based on the LHS method. CFD simulation is conducted using the coupled turbulence-combustion model combining the EDC model with the simplified combustion reaction mechanism. The sample points and calculation results are used as the total dataset. 65 sets of data are used to create the model, and 25 sets of data are used to test the performance. Each set of data in the dataset consists of five-dimensional data, including the excess air coefficient, fuel gas flow rate, air preheating temperature, outlet NO_x concentration, and thermal efficiency of the firebox.

The input variables of the RBF neural network are selected as the first three-dimensional parameters of each sample, and their mathematical descriptions are $x = (x_1, x_2, x_3)^T$. The outputs of the neural network $y = (y_1, y_2, y_3)^T$ are the outlet NO_x concentration and thermal efficiency of the firebox. The network is set as a three-layer forward network, that is, the number of neurons in the input layer is 3, in the output layer – 2, and its number in the hidden layer is the same as the number of training samples, which is 65. To ensure the accuracy and generalization ability of the network model, the data samples are normalized. The structure of the RBF neural network based on cracking furnace combustion is shown in Fig. 7.

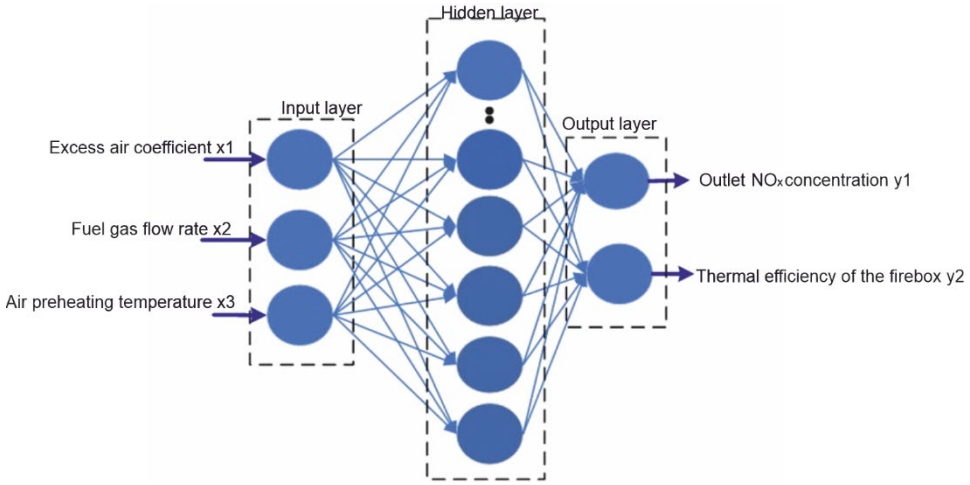

Fig. 7. Structure of the RBF neural network of cracking furnace combustion

The hidden layer maps each low-dimensional input vector in the input space to the high-dimensional space through an activation function, which transforms the problem of low-dimensional linear inseparability into a problem of linear separability. In this work, the Gaussian function is selected as the activation function. After the input vector x enters the hidden layer, a radial basis transform occurs:

$$g_i = \exp\left(-\frac{\|x - c_i\|^2}{2\sigma_i^2}\right), \quad \sigma_i > 0, \ 1 \le i \le n \tag{16}$$

where g_i is the output of the ith hidden layer neuron, $\|\cdot\|$ represents the Euclidean distance from the input vector to the center point, $\mathbf{c}_i$ represents the center vector of the ith hidden layer neuron; σ_i represents the base width of the ith neuron in the hidden layer, and n is the number of neurons in the hidden layer.

The mapping from the hidden layer to the output layer is linear, and the final output result of the network is the linear weighted sum of each neuron in the hidden layer, which can be expressed as:

$$y_k = \omega_{k,0} + \sum_i^n \omega_{k,i}\, g\left(\|x - c_i\|^2\right), \quad k = 1, 2, \ 1 \le i \le n \tag{17}$$

where y_k is the output of the kth neuron in the output layer, and all outputs form the output matrix $\mathbf{y} = [y_1, y_2, \ldots, y_n]^T$; $\omega_{k,0}$ is the deviation value of the kth neuron in the output layer, $\omega_{k,i}$ is the connection weights of the ith neuron in the hidden layer and the kth neuron in the output layer.

For RBF neural networks, the key to training is the selection of the center point of the basis function. This paper uses the *K*-means clustering algorithm to select the center point. In this algorithm, several sets of sample data are randomly selected as the initial clustering centers. Then, based on the response degree of the kernel function between each input sample and the clustering center, they are assigned to the corresponding range of clustering center points. The larger the response degree, the closer the distance is. Each center point and its contained samples are a cluster. During each sample allocation process, each cluster accountant calculates the average value of all its internal samples as the new cluster center point until the iteration stops. The base widths of each basis function at the center point can be obtained from the equation

$$\sigma_i = \frac{d_{\max}}{\sqrt{2n}} \tag{18}$$

where $d_{\max}$ is the maximum distance between the selected center points.

The gradient descent method is used to train weights, and the loss function is the root mean square error (RMSE):

$$E = \sqrt{\frac{\sum_{i=1}^{N}\sum_{j=1}^{K}(\hat{y}_{ij} - y_{ij})^2}{N}} \tag{19}$$

where $\hat{y}_{ij}$ is the predicted value of the neural network, and y_{ij} is the actual value.

The termination target value ε is set to 0.0001. If the value of the loss function E is less than ε after multiple iterations, the training stops. Otherwise, the iteration continues until convergence is obtained.

4.3.2. SUPPORT VECTOR REGRESSION – SVR

SVR is a regression algorithm developed based on the support vector machines (SVM). SVR minimizes the total deviation of sample points from the hyperplane by searching for hyperplanes rather than separating sample points of different categories as much as possible. Due to the use of kernel functions to map low-dimensional input vectors into high-dimensional feature spaces, SVR can produce better prediction results than traditional regression algorithms when processing nonlinear data. It has also a stronger generalization ability.

Specifically, if the sample set $D = \{(x_1, y_1), (x_2, y_2), \ldots, (x_m, y_m)\}$ is given, and the form of the decision surface equation is $f(x_i) = \omega x_i + b$, where ω is the weight vector which determines the direction of the decision surface, b is the bias constant term that determines the position of the decision surface. Meanwhile, SVR assumes that we can tolerate a maximum of the error ε between model output $f(x_i)$ and actual output y_i. Only

when the absolute value of the difference between $f(x_i)$ and y_i is greater than ε is the loss calculated.

Thus the SVR problem can be written as

$$\min_{\omega,\, b} \frac{1}{2}\|\omega\|^2 + C\sum_{i=1}^{m} l_\varepsilon\left(f(x_i) - y_i\right) \tag{20}$$

$$\text{s.t.} \quad \begin{cases} y_i - f\left(x_i\right) \le \varepsilon \\ f\left(x_i\right) - y_i \le \varepsilon \end{cases}, \; i = 1, 2, ..., m \tag{21}$$

where m is the number of samples, C is the regularization constant, and l_ε represents the ε-insensitive loss function.

$$l_\varepsilon(z) = \begin{cases} 0, |z| < \varepsilon \\ |z| - \varepsilon \text{ otherwise} \end{cases} \tag{22}$$

where $|z|$ is the distance from the sample point to the decision surface which can be expressed as $|y_i - f(x_i)|$.

To solve the problem beyond width range of the error ε, slack variables ξ_i, ξ_i^* are introduced. Then Eq. (20) is rewritten as:

$$\min_{\omega, b, \xi_i, \xi_i^*} \frac{1}{2}\|\omega\|^2 + C\sum_{i=1}^{m}\left(\xi_i + \xi_i^*\right) \tag{23}$$

$$\text{s.t.} \begin{cases} y_i - f(x_i) \le \varepsilon + \xi_i \\ f(x_i) - y_i \le \varepsilon + \xi_i^* \\ \xi_i, \xi_i^* \ge 0, \; i = 1, 2, ..., m \end{cases} \tag{24}$$

Let us introduce Lagrangian multipliers $\mu_i \ge 0, \mu_i^* \ge 0, \alpha \ge 0, \alpha^* \ge 0$ to obtain the following Lagrangian function:

$$L\left(\omega, b, \alpha, \alpha^*, \xi, \xi^*, \mu, \mu^*\right) = \frac{1}{2}\|\omega\|^2 + C\sum_{i=1}^{m}\left(\xi_i + \xi_i^*\right) - \sum_{i=1}^{m}\mu_i\xi_i - \sum_{i=1}^{m}\mu_i^*\xi_i^*$$

$$-\sum_{i=1}^{m}\alpha_i\left(f(x_i) - y_i + \varepsilon + \xi_i\right) - \sum_{i=1}^{m}\alpha_i^*\left(y_i - f(x_i) + \varepsilon + \xi_i^*\right) \tag{25}$$

There are the following equations at the optimal solution

$$\begin{cases} \dfrac{\partial L}{\partial \omega} = \omega - \sum\limits_{i=1}^{m} (\alpha_i - \alpha_i^*) x_i = 0 \\ \dfrac{\partial L}{\partial b} = \sum\limits_{i=1}^{m} (\alpha_i^* - \alpha_i) = 0 \\ \dfrac{\partial L}{\partial \xi_i} = C - \alpha_i - \mu_i = 0 \\ \dfrac{\partial L}{\partial \xi_i^*} = C - \alpha_i^* - \mu_i^* = 0 \end{cases} \tag{26}$$

By substituting Eq. (25) into Eq. (26), the original problem can be transformed into its dual problem:

$$\begin{cases} \max\limits_{\alpha, \alpha^*} \sum\limits_{i=1}^{m} y_i (\alpha_i - \alpha_i^*) - \varepsilon (\alpha_i^* + \alpha_i) - \dfrac{1}{2} \sum\limits_{i=1}^{m} \sum\limits_{j=1}^{m} (\alpha_i - \alpha_i^*)(\alpha_j - \alpha_j^*)(x_i^T x_j) \\ \text{s.t.} \begin{cases} \sum\limits_{i=1}^{m} (\alpha_i - \alpha_i^*) = 0 \\ \alpha_i^* \geq 0, \quad \alpha_i \leq C \end{cases} \end{cases} \tag{27}$$

By solving the above equation, the regression function can be obtained

$$f(x) = \sum_{i=1}^{m} (\alpha_i - \alpha_i^*) x_i^T x + b \tag{28}$$

For nonlinear problems, a mapping relationship $\phi(x)$ from low to high dimensions can be introduced to make the problem linearly separable. At the same time, a kernel function $k(x_i, x_j) = \phi(x_i)^T \phi(x_j)$ can be defined to achieve non-spatial transformation without knowing the specific form of $\phi(x)$, solving the problem of possible dimensionality disasters. For SVR problems that use kernel techniques, they can be expressed as:

$$f(x) = \sum_{i=1}^{m} (\alpha_i - \alpha_i^*) k(x_i, x) + b \tag{29}$$

To ensure sample consistency, the SVR combustion model uses the same dataset as the RBF neural network and normalizes the training and testing data. The SVR model

is established based on Matlab2019b software. For the complex combustion environment in the firebox, the influencing factors of thermal efficiency of the firebox and NO_x emission concentration are coupled with each other, and there is a strong nonlinear relationship between input and output. Therefore, a Gaussian kernel function with strong nonlinear mapping ability is selected as the kernel function of the SVR, which can effectively solve the determination and optimization of algorithm parameters. However, it is necessary to adjust the coefficient Gamma. This coefficient invisibly determines the distribution of the data after being mapped to the new feature space. The larger the Gamma, the fewer the support vectors, and the more susceptible the model is to the influence of individual samples, which can easily lead to a decrease in the prediction accuracy of the model for the test samples, resulting in overfitting problems. On the contrary, the smaller the gamma value, the easier it is for the model to have insufficient prediction accuracy for the training samples, resulting in poor fitting problems. In addition, it is necessary to adjust the penalty parameter C, which represents the acceptable range of error between the predicted value and the true value of the model. If the value of C is too large or too small, it will seriously affect the prediction accuracy and generalization ability of the model. The training process of this model adopts the k-fold cross-validation method to optimize the model parameters, where $k = 5$.

4.3.3. COMPARISON OF DIFFERENT SURROGATE MODELS FOR CRACKING FURNACES

Figures 8 and 9 show simulation effects of testing samples for NO_x emission concentration and thermal efficiency of the firebox, respectively. The simulation results show that the average relative error of outlet NO_x concentration of the test samples between the RBF neural network model and CFD model is 1.25%, with a maximum relative error of 3.65%. In contrast, the average relative error of outlet NO_x concentration of the test samples between the SVR model and CFD model is 1.24%, with a maximum relative error of 4.3%. The average relative error of thermal efficiency of the test samples between the RBF neural network model and CFD model is 0.053%, with a maximum relative error of 0.38%.

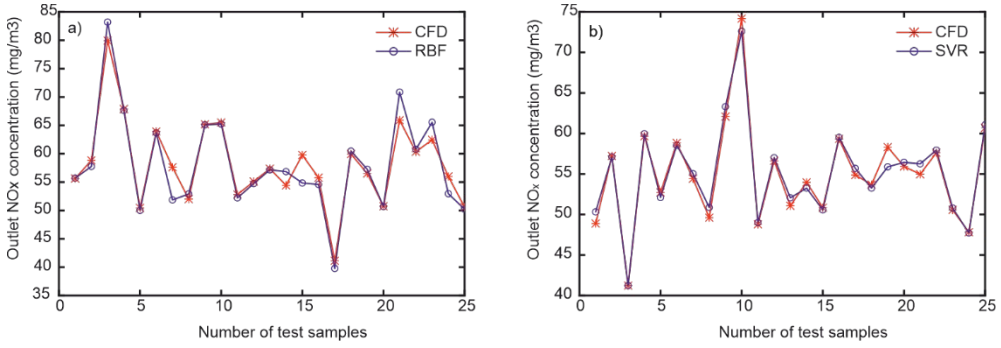

Fig. 8. Predicted NO_x concentration with RBF (a) and SVR (b) models

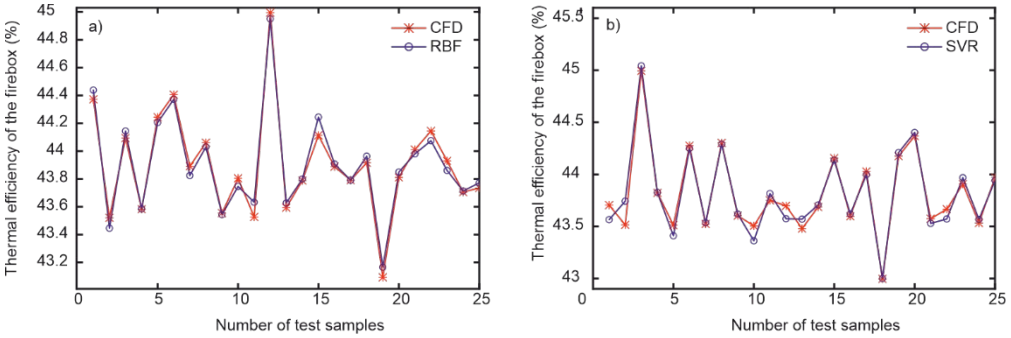

Fig. 9. Predicted thermal efficiency of the firebox with RBF (a) and SVR (a) models

By comparison, the average relative error of thermal efficiency of the test samples between the SVR model and CFD model is 0.15%, and the maximum relative error is 0.68%. It can be seen that the RBF neural network model is a better choice for building a prediction model for the combustion characteristics of the cracking furnace compared to SVR model.

To quantitatively compare the simulation performance and generalization ability of the RBF neural network and SRV model, mean square error (MSE), RMSE and the coefficient of determination (R^2) are used to evaluate:

$$\mathrm{MSE}(y, \hat{y}) = \frac{1}{m}\sum_{i=1}^{m}(y_i - \hat{y}_i)^2 \tag{30}$$

$$\mathrm{RMSE}(y, \hat{y}) = \sqrt{\frac{1}{m}\sum_{i=1}^{m}(y_i - \hat{y}_i)^2} \tag{31}$$

$$R^2 = 1 - \frac{\sum_{i=1}^{m}(y_i - \hat{y}_i)^2}{\sum_{i=1}^{m}(y_i - \bar{y})^2} \tag{32}$$

where $\bar{y}$ is the average of the true values. The closer R^2 to 1, the better performance of the model and the closer R^2 to 0, the worse performance of the model is.

Table 4

Indicators for the NO outlet concentration predicted for different models

Model	MSE	RMSE	R^2
RBF	1.518	1.2321	0.98808
SVR	1.915	1.3968	0.98379

Table 5

Indicators for thermal efficiency predicted for the firebox of different models

Model	MSE	RMSE	R^2
RBF	0.0024	0.0489	0.99608
SVR	0.0076	0.0869	0.98585

The sample evaluation indicators for the NO outlet concentration prediction of different models are shown in Table 4, the sample evaluation indicators for thermal efficiency prediction of the firebox of different models are shown in Table 5. The simulation accuracy and R^2 of the RBF neural network are better than those of the SVR model with better simulation and generalization capabilities. It has better targeting in terms of NO_x outlet concentration and thermal efficiency of the firebox. Therefore, the RBF neural network is selected as the fast response surrogate model for cracking furnace combustion.

4.4. MULTI-OBJECTIVE OPTIMIZATION FOR RAPID RESPONSE TO COMBUSTION

This study is based on the NSGA-II algorithm. The outlet NO_x concentration and thermal efficiency of the firebox are selected as the objective functions for multi-objective optimization of cracking furnace combustion. The RBF neural network is used as the prediction model for furnace combustion characteristics of this optimization algorithm. The multi-objective decision model can be summarized as follows:

$$\hat{Y}_{\mathrm{NO}_x} = \min \mathrm{X}_{\mathrm{NO}_x}(a, q, T) \tag{33}$$

$$\hat{Y}_{\eta_{\mathrm{fire}}} = \max X_{\eta_{\mathrm{fire}}}(a, q, T) \tag{34}$$

$$\text{s.t.} \begin{cases} q_{\min} \le q \le q_{\max} \\ a_{\min} \le a \le a_{\max} \\ T_{\min} \le T \le T_{\max} \end{cases} \tag{35}$$

where a is the excess air coefficient, q is the fuel gas flow rate, and T is the air preheating temperature. The range of decision variables is the same as that in Section 4.2.

To fully explore the search space and obtain better solutions, this algorithm adopts real number encoding and selects a binary tournament selection operator. The simulated binary crossover (SBX) is used as a crossover operator, and the crossover probability is set to 1. The polynomial mutation is selected as the mutation operator. Due to the number of decision variables involved in this study being 3, the mutation probability is set

to 1/3. In the experiment, the population size is set to 100 and the maximum number of iterations is 500. To avoid the influence of accidental factors as much as possible, the NSGA-II program is run 30 times and its average value is taken, as shown in Fig. 10. The final result is a Pareto front composed of 38 different optimized individuals.

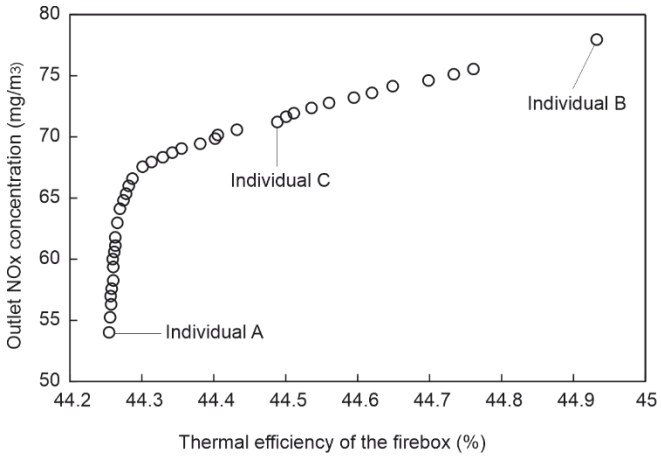

Fig. 10. Pareto front with NSGA-II optimization algorithm

The outlet NO_x concentration range optimized by the NSGA-II algorithm is between 54 and 79 mg/m^3, and the range of thermal efficiency of the firebox is between 44.2 and 44.9%. In addition, it can be verified that there is a significant conflict between the thermal efficiency of the firebox and the outlet NO_x concentration due to the ultra-low nitrogen combustion strategy. Due to the non-dominated feature of the NSGA-II algorithm, the program does not provide the optimal operating parameters. To comprehensively consider the thermal efficiency of the firebox and NO_x emissions, this study selects individual A located at the lower left, individual C located at the upper right, and individual B located between individual A and individual C for analysis and comparison to obtain the optimal operating scheme. The specific operating parameters are shown in Table 6.

Table 6

Operating parameters of optimized individuals A, B, and C

Optimized individual	Excess air coefficient	Fuel gas flow rate [kg/s]	Air preheating temperature [K]	Outlet NO_x concentration [mg/m^3]	Thermal efficiency of the firebox [%]
Individual A	1.03	0.217	330	54.0	44.25
Individual B	1.07	0.192	380	71.2	44.49
Individual C	1.09	0.189	392	78.1	44.93
Original scheme	1.1	0.18	325	75.38	43.82

For optimized individual A, although the outlet NO_x is only 54.0 mg/m^3, which corresponds 28.36% decrease compared to the original scheme, the thermal efficiency of the firebox is not outstanding compared to other individuals. Although the thermal efficiency of the firebox of individual C reaches 44.93% which is increased by 2.53% compared to the original scheme, the outlet NO_x concentration reaches 78.1 mg/m^3 which is not the best NO_x emission scheme either. Therefore, considering emission reduction and energy conservation indicators, individual B is the most ideal individual. Compared to the original scheme, its NO_x emission has been reduced by 5.55%, and the thermal efficiency of the firebox has been improved by 1.53%. He [34] indicated that a 0.1% increase in thermal efficiency can increase ethylene production by 6.2% in a naphtha-cracking furnace. The thermal efficiency of the cracking furnace increases by about 1%, which is equivalent to an energy saving of 7.143 kg of standard coal/ton of ethylene. Therefore, the optimized furnace thermal efficiency in this study can bring a significant economic benefit to ethylene manufacturing.

5. CONCLUSION

This paper proposed a multi-objective optimization scheme of the ultra-low nitrogen burners which combines CFD numerical simulation based on the simplified reaction mechanism with machine learning methods to establish a strong generalization-based turbulent combustion surrogate model. The major conclusions are described as follows:

The EDC model is coupled with GRI 3.0 reaction kinetics, and the turbulent combustion coupling model is further established for the cracking furnace. Detailed information on the velocity, temperature, and concentration fields of flue gas is obtained, and the impact of combustion characteristics in the cracking furnace on NO_x generation is analyzed.

The DRG method is combined with the CSP method and a simplified mechanism involving 29 species and 164 reactions is obtained. The simplified mechanism is validated in three-dimensional numerical simulations using the Sandia Flame D. The results show that the simplified mechanism can achieve accurate prediction of the temperature field, velocity field, and concentration of each component while reducing the computational time by about 60%.

By taking the RBF neural network as the intermediate model, the NGSA-II algorithm is used to realize the multi-objective optimization of NO_x emissions and thermal efficiency of the firebox, and a Pareto solution set that meets the expectations is obtained. Simulation results show that considering NO_x emission reduction and energy conservation indicators, the optimal operating parameter scheme, i.e., excess air coefficient of 1.07, fuel gas flow rate of 0.192 kg/s, and air preheating temperature of 380 K, reduces the NO_x emission concentration from 75.38 to 71.2 mg/m^3, i.e., a decrease of 5.55%. The thermal efficiency of the firebox increased from 43.82% to 44.49%, i.e., an increase of

1.53%, which provides a theoretical guide for the economic and environmental protection operation of cracking furnaces.

For future work, the reactor tubes of the ethylene cracking furnace will be considered. A high-fidelity turbulent combustion coupling model will be constructed to meet the requirements of NO_x emissions and industrial equipment heat load. This can broaden the selection range of decision variables and change the optimization objective to the overall furnace thermal efficiency rather than the thermal efficiency of the firebox.

ACKNOWLEDGMENTS

This work was supported by the National Natural Science Foundation of China (Basic Science Center Program: 61988101), the National Natural Science Foundation of China (62273149, 62173144), and Fundamental Research Funds for the Central Universities.

REFERENCES

[1] WANG D.F., LIU Q., HAN P., ZHAO W.J., *Combustion optimization in power station based on big data-driven case-matching*, Chin. J. Sci. Instrum., 2016, 37 (2), 420–428. DOI: 10.19650/j.cnki.cjsi.2016.02.024.

[2] SCHLUCKNER C., GABER C., LANDFAHRER M., DEMUTH M., HOCHENAUER C., *Fast and accurate CFD model for NO_x emission prediction during oxy-fuel combustion of natural gas using detailed chemical kinetics*, Fuel, 2020, 264, 116841. DOI: 10.1016/j.fuel.2019.116841.

[3] NIE Z.B., *Application and effect analysis of CFD numerical simulation technology in the transformation of low nitrogen burner in cracking furnace*, Henan Chem. Ind., 2018, 35 (05), 41–44. DOI: 10.14173/j.cnki.hnhg.2018.05.011.

[4] SHANOCK L.R., BARAN B.E., GENTRY W.A., PATTISON S.C., HEGGESTAD E.D., *Polynomial regression with response surface analysis. A powerful approach for examining moderation and overcoming limitations of difference scores*, J. Bus. Psychol., 2010, 25 (4), 543–554. DOI: 10.1007/s10869-010-9183-4.

[5] OLIVER M.A., WEBSTER R., *Kriging. A method of interpolation for geographical information systems*, Int. J. Geogr. Inf. Syst., 1990, 4 (3), 313–332.

[6] SMOLA A.J., SCHÖLKOPF B., *A tutorial on support vector regression*, Stat. Comput., 2004, 14, 199–222. DOI: 10.1023/B:STCO.0000035301.49549.88.

[7] CUI K., JING X., *Research on prediction model of geotechnical parameters based on BP neural network*, Neural Comput. Appl., 2019, 31, 8205–8215. DOI: 10. 1007/s00521-018-3902-6.

[8] KARAYIANNIS N.B., MI G.W., *Growing radial basis neural networks. Merging supervised and unsupervised learning with network growth techniques*, IEEE T. Neural Net., 1997, 8 (6), 1492–1506. DOI: 10.1109/72.641471.

[9] GU J., WANG Z., KUEN J., MA L., SHAHROUDY A., SHUAI B., LIU T., WANG X., WANG G., CAI J., CHEN T., *Recent advances in convolutional neural net*works, Pattern Recogn., 2018, 77, 354–377. DOI: 10.1016/j.patcog.2017.10.013.

[10] BROWN D.G., RIOLO R., ROBINSON D.T., NORTH M., RAND W., *Spatial process and data models. Toward integration of agent-based models and GIS*, J. Geogr. Syst., 2005, 7 (1), 25–47. DOI: 10.1007/s10109-005-0148-5.

[11] ABOABA A., MARTINEZ Y., MOHAGHEGH S., SHAHNAM M., GUENTHER C., LIU Y., *Smart proxy modeling application of artificial intelligence and machine learning in computational fluid dynamics*, National Energy Technology Laboratory (NETL), Pittsburgh, PA, 2020.

[12] YAO Q., ZHANG Y., WANG X., TIAN Z., HU G., DU W., *Investigation of NO_x emission under different burner structures with the optimized combustion model*, Neurocomp., 2022, 482, 224–235. DOI: 10.1016/j.neucom.2021.11.051.
[13] YUAN B., MA J.G., CHEN D., *Modification and operation adjustment of low nitrogen oxide burner in cracking furnace*, Ethyl. Ind., 2018, 30 (2), 35–38.
[14] MARLER R.T., ARORA J.S., S*urvey of multi-objective optimization methods for engineerin*g, Struct. Multidisc. O., 2004, 26, 369–395. DOI: 10.1007/s00158-003-0368-6.
[15] GOEL H.D., GRIEVINK J., HERDER P.M., WEIJNEN M.P.C., *Integrating reliability optimization into chemical process synthesis*, Reliab. Eng. Syst. Safe., 2002, 78 (3), 247–258. DOI: 10.1016/S0951-8320 (02)00167-9.
[16] MENZEL G., OCH S.H., MARIANI V.C., MOURA L.M., DOMINGUES E., *Multi-objective optimization of the volumetric and thermal efficiencies applied to a multi-cylinder internal combustion engine*, Energ. Convers. Manage., 2020, 216, 112930. DOI: 10.1016/j.enconman.2020.112930.
[17] SENER R., GÜL M.Z., *Optimization of the combustion chamber geometry and injection parameters on a light-duty diesel engine for emission minimization using multi-objective genetic algorithm*, Fuel, 2021, 304, 121379. DOI: 10.1016/j.fuel.2021.121379.
[18] SMITH G.P., GOLDEN D.M., FRENKLACH M., MORIARTY N.W., EITENEER B., GOLDENBERG M., BOWMAN C.T., HANSON R.K., SONG S., GARDINER W.C., LISSIANSKI V.V., QIN Z., *GRI-Mech, version 3.0*, http://www.me.berkeley.edu/gri_mech/.2002.
[19] Ansys, Inc., *ANSYS Fluent Theory Guide 19.1*, Canonsburg, PA, 2018.
[20] HU G.H., WANG H.G., QIAN F., *Numerical simulation on flow, combustion and heat transfer of ethylene cracking furnace*s, Chem. Eng. Sci., 2011, 66 (8),1600–1611. DOI: 10.1016/j.ces.2010.12.028.
[21] FRASSOLDATI A., SHARMA P., CUOCI A., FARAVELLI T., RANGI E., *Kinetic and fluid dynamics modeling of methane/hydrogen jet flames in diluted coflow*, Appl. Therm. Eng., 2010, 30 (4), 376–383. DOI: 10.1016/ j.applthermaleng.2009.10.001.
[22] ZELDOVICH J., *The oxidation of nitrogen in combustion and explosions*, Acta Phys., 1946, 21 (4), 577–628.
[23] HABIBI A., MERCI B., HEYNDERICKX G.J., *Multiscale modeling of turbulent combustion and NO_x emission in steam crackers*, AIChE J., 2007, 53, 2384–2398. DOI: 10.1002/aic.11243.
[24] DENISON M.K., WEBB B.W., *Spectral line-based weighted-sum-of-gray-gases model for arbitrary RTE solvers*, J. Heat Trans-T. ASME, 1993, 115 (4), 1004–1012.
[25] KEE R.J., RUPLEY F.M., MILLER J.A., COLTRIN M.E., GRCAR J.F., MEEKS E., MOFFAT H.K., LUTZ A.E., DIXON-LEWIS G., SMOOKE M.D., WARNATZ J., EVANS G.H., LARSON R.S., MITCHELL R.E., PETZOLD L.R., REYNOLDS W.C., CARACOTSIOS M., STEWART W.E., GLARBORG P., WANG C., ADIGUN O., HOUF W.G., CHOU C.P., MILLER S.F., HO P., YOUNG D.J., *CHEMKIN Release 4.0*, Reaction Design, Inc., San Diego, CA, 2004.
[26] SAINI R., PRAKASH S., DE A., YADAV R., *Investigation of NO_x in piloted stabilized methane-air diffusion flames using finite-rate and infinitely-fast chemistry based combustion models*, Therm. Sci. Eng. Prog., 2018, 5, 144–157. DOI: 10.1016/ j.tsep.2017.11.008.
[27] LAN X.Y., GAO J.S., XU C.M., ZHANG H.M., *Numerical simulation of transfer and reaction processes in ethylene furnaces*, Chem. Eng. Res. Des., 2007, 85 (A12),1565–1579. DOI: 10.1205/cherd07008.
[28] XU Q., CHEN B.Z., HE X.R., ZHANG L., *Simulation for naphtha pyrolysis in clear radiation tube of SRT-IV cracking furnace*, Comp. Appl. Chem., 2001, 18 (3), 223–228. DOI: 10.16866/j.com.app.chem2001.03.007.
[29] ZHANG J., LI J.K., *NO_x suppression technology for cracking furnace*, Ethylene Ind., 2013, 25 (4), 40–43.
[30] ZHANG K., *The analysis and optimization of Daqing ethylene cracking furnace thermal efficiency*, Jiangxi Chem. Ind., 2015, 2 (2), 17–20.
[31] WANG P., *More fuel gas boiler combustion adjustment and operation optimization*, Changsha University of Science and Technology, Changsha 2015.
[32] ZHANG Z.C., GAO T.Y., ZHANG L., TUO S.F., *Aeroheating agent model based on radial basis function neural network*, Acta Aeronaut. Astronaut. Sin., 2021, 42 (2), 524167. DOI: 10.7527/S10000-6893.2020.24167.

[33] CHEN T.L., *Application of support vector regression in thickness prediction of tectonic coal*, China University of Mining and Technology, Xuzhou 2021.
[34] HE X., *Development and application of Sinopec CBL large capacity cracking furnace*, Ethylene Ind., 2015, 27 (1), 49–52.